Y$_3$Fe$_{0.5}$SiSe$_7$: A new cation-deficient quaternary mixed transition metal chalcogenide with extremely low thermal conductivity

Gopabandhu Panigrahi [a], Sweta Yadav [a], Subhendu Jana [a], Muthukumaran Sundaramoorthy [b], Sonachalam Arumugam [b], Manish K. Niranjan [c], Jai Prakash [a],[*]

[a] Department of Chemistry, Indian Institute of Technology Hyderabad, Kandi, Sangareddy, Telangana, 502284, India
[b] Centre for High Pressure Research, School of Physics, Bharathidasan University, Tiruchirapalli, 620024, India
[c] Department of Physics, Indian Institute of Technology Hyderabad, Kandi, Sangareddy, Telangana, 502284, India

A B S T R A C T

Single crystals of a new selenide, Y$_3$Fe$_{0.5}$SiSe$_7$, have been synthesized by a reaction of elements at high temperatures inside a vacuum-sealed fused silica tube. The title phase crystallizes in the hexagonal non-centrosymmetric $P6_3$ space group (Pearson symbol $hP23$) at room temperature (RT), as established by a single-crystal X-ray diffraction study. The structure is non-stoichiometric with refined lattice parameters of $a = b = 10.1971(1)$ Å, $c = 5.9799(2)$ Å, and $V = 538.49(2)$ Å^3 ($Z = 2$). The asymmetric unit of the structure consists of six crystallographically independent atomic positions: one Y, one half-occupied Fe, one Si, and three Se sites. The building blocks of the structure are a distorted FeSe$_6$ octahedron, YSe$_6$ trigonal prism, and SiSe$_4$ tetrahedron that are fused together via sharing of anions to create a three-dimensional periodic network. The charge-balanced formula of the structure can be achieved as $(Y^{3+})_3(Fe^{2+})_{0.5}(Si^{4+})_1(Se^{2-})_7$. A polycrystalline sample of Y$_3$Fe$_{0.5}$SiSe$_7$ was also synthesized by the high-temperature reactions of stoichiometric amounts of elements. A direct bandgap value of 1.1(1) eV for the polycrystalline sample was estimated by a solid-state UV–Vis–NIR absorption spectroscopic study. A resistivity study on the polycrystalline Y$_3$Fe$_{0.5}$SiSe$_7$ sample corroborates its semiconducting nature. The polycrystalline sample also shows an extremely low thermal conductivity value of ~0.26 Wm^{-1}K^{-1} at 773 K. The *ab-initio* optical and thermoelectric parameters of the title structure have been estimated from the electronic band structure. The relative bond strengths of Y, Si, and Fe atoms with Se atoms are investigated by the COHP study.

1. Introduction

The field of exploratory syntheses of new metal chalcogenides is of utmost importance for solid-state and materials scientists when it comes to the design and discovery of new functional materials with captivating structural-property relationships [1–3]. Metal chalcogenides that crystallize in the noncentrosymmetric space groups are promising for nonlinear optical (NLO) applications [4,5]. Over the last few decades, many such new noncentrosymmetric chalcogenide materials have been synthesized, and a few of these members that show remarkably high nonlinear optical responses were identified [6]. A few examples of noncentrosymmetric metal chalcogenides are Sn$_2$Ga$_2$S$_5$ [7], BaHgSe$_2$ [8], In$_2$Se$_3$ [9], Y$_6$ZnSi$_2$S$_{14}$ [10], Ba$_2$Ge$_2$Te$_5$ [11], and M_2As$_2Q_5$ (M = Ba, Pb; Q = S, Se) [12]. Among these, the chalcogenides with smaller bandgap values are the most promising candidates for infrared lasers

that have numerous applications in security, visualization, and environmental monitoring [13]. These noncentrosymmetric chalcogenides consist of transition metals or main-group elements or both, along with chalcogens (Q = S, Se, and Te). Transition metal chalcogenides are not only limited to NLO applications but are also known for other potential applications such as magnetic [14], thermoelectric properties [15], ion exchange [16], and superconductivity [17]. Thus, one of the critical areas of modern material sciences is the production of new inorganic crystalline compounds with increasingly complicated compositions and unique properties, such as ternary, quaternary, and higher-order mixed metal chalcogenides.

Many noncentrosymmetric quaternary chalcogenide compounds with the general formula $Ln_3MM'Q_7$ and $Ln_3M_{0.5}M'Q_7$ have been reported (Ln = Y or lanthanides; M = monovalent or divalent transition metal; M' = main group elements; and Q = chalcogens) in the literature

[18–21]. Due to their remarkable structural flexibility and appealing optical properties, these quaternary metal chalcogenides with three-dimensional (3D) noncentrosymmetric frameworks are potential candidates for IR-NLO applications [22]. From a structural point of view, these compounds consist of a positive moiety acting as a charge-balancing unit (and space filler) and a 3D framework of negative moiety acting as the main building blocks of the structures. The M and M' metals in the $Ln_3MM'Q_7$ and $Ln_3M_{0.5}M'Q_7$ compounds contribute a total charge contribution of +5 in the (3 + 2) and (1 + 4) manner, respectively. The latter type of metal combination leads to vacancies at the M sites, and the extent of vacancy is dependent on the oxidation states of the M and M' atoms. For example, half of the M sites are vacant in the case of the $La_3Fe_{0.5}SiSe_7$ [23], where the Fe atoms are present in the +(II) oxidation state. These two families of compounds with general compositions of the $Ln_3MM'Q_7$ and $Ln_3M_{0.5}M'Q_7$ host a wide range of transition (M) and main-group metals (M'). All independent crystallographic sites of main group triel (Tr = Al, Ga, and In) containing Ln_3MGaQ_7 (M = Fe, Co, Ni; Q = S, Se) [18] compounds are fully occupied while the presence of main group tetrel (Tt = Si and Ge) elements in the $Ln_3M_{0.5}TtSe_7$ (Ln = La, Ce, Sm; M = Fe, Mn) [23] requires half-occupied M sites to maintain the electrical neutrality of the composition. Incorporating monovalent transition metals like Cu^{1+} in the $Ln_3M_{0.5}TtSe_7$ stabilizes stoichiometric compounds such as the $La_3CuGeSe_7$ [24]. The stabilization of these structures without Ln^{3+} is also possible by replacing these cations with Y^{3+} and Sc^{3+} species. The possibility of midgap states which have a detrimental impact on the enlargement of bandgaps of such structures, which do not have valence d (or full d^{10} configurations, e.g., Cu^{1+}) or f-electrons, can be avoided due to lack of the d-d or f-f electronic transitions. Therefore, the bandgap of these compounds can be fine-tuned easily by the proper choice of metals in their structures to optimize their NLO properties.

In this article, we present the synthesis and characterization of a new mixed transition metals quaternary chalcogenide $Y_3Fe_{0.5}SiSe_7$. The traditional high-temperature reactions of elements in sealed fused silica tubes are used for the synthesis of both single-crystals and a polycrystalline phase of the $Y_3Fe_{0.5}SiSe_7$. The crystal structure of this non-stoichiometric compound is determined using a single-crystal X-ray diffraction study. We have also investigated the UV–vis–NIR absorbance spectroscopic and low-temperature resistivity studies on the polycrystalline sample of $Y_3Fe_{0.5}SiSe_7$. The thermal conductivity of the polycrystalline $Y_3Fe_{0.5}SiSe_7$ compound was also thoroughly investigated over a wide temperature range, along with theoretical thermoelectric properties calculated via the *ab initio* DFT method.

2. Experimental

2.1. Materials used and synthesis methodology

We have used the following chemicals for the synthesis of the crystals and the polycrystalline samples of the $Y_3Fe_{0.5}SiSe_7$: yttrium rod (99.9%, Alfa Aesar), iron granules (99.98%, Alfa Aesar), silicon granules (99.99%, Alfa Aesar), and selenium powder (99.5%, Sigma Aldrich). The yttrium rod was shredded into coarse particles before use. All the chemicals were loaded into carbon-coated tubes inside an argon-filled dry glove box.

2.1.1. Synthesis of the single crystals of the $Y_3Fe_{0.5}SiSe_7$

A high-temperature reaction of corresponding elements produced the block-shaped, black-colored crystals of the $Y_3Fe_{0.5}SiSe_7$. All the elements, Y (60.9 mg, 0.685 mmol), Fe (6.4 mg, 0.114 mmol), Si (6.4 mg, 0.224 mmol), and Se (126.2 mg, 1.599 mmol), were transferred into a carbon-coated fused silica tube, and then the tube was flame-sealed after evacuation ($\sim 10^{-4}$ Torr) using a diffusion vacuum pump. The sealed ampule was first heated to 923 K in 12 h inside a muffle furnace and annealed for 12 h before ramping the furnace's temperature to 1223 K with a heating rate of 20 K/h. The furnace's temperature was held

constant for 72 h at 1223 K, then cooled down to 573 K at a rate of 4 K/h. Finally, the furnace was shut off, and the reaction mixture was cooled radiatively to RT.

A black ingot was obtained after breaking the heat-treated ampoule under the ambient environment. The ingot was crushed and analyzed under an optical microscope. A few crystals were selected and subjected to elemental analysis using a semi-quantitative energy dispersive X-ray (EDX) spectroscopic study. The EDX data (Fig. 1a) revealed the presence of Y, Fe, Si, and Se in a ~3.05:0.49:1.0:7.2 ratio, corresponding to the $Y_3Fe_{0.5}SiSe_7$ formula. The EDX studies were carried out with the aid of an octane elite (EDAX Inc., USA) spectrometer that was attached to a field emission scanning electron microscope (FE-SEM) model number JSM 7800 F (Make: JEOL, Japan). The EDX data were collected using a 20 kV accelerating voltage.

2.1.2. Synthesis of the polycrystalline $Y_3Fe_{0.5}SiSe_7$ phase

The high-temperature solid-state sealed tube method was used to synthesize a polycrystalline sample of $Y_3Fe_{0.5}SiSe_7$. In a carbon-coated fused silica tube, the reactants Y, Fe, Si, and Se were loaded with the molar ratio of 3:0.5:1:7. The total mass of the reactants was 1 g: Y (304.5 mg, 3.426 mmol), Fe (31.9 mg, 0.571 mmol), Si (32.1 mg, 1.142 mmol), and Se (631.3 mg, 7.995 mmol). The vacuum-sealed tube containing the reaction mixture was heat treated inside the furnace. The temperature of the furnace was raised to 523 K in 12 h from RT and dwelled there for 12 h. Further, the temperature was ramped to 1173 K (in 24 h), and the reaction mixture was annealed for 96 h before switching off the furnace.

The product formed in the first step of the reaction was homogenized into a fine powder inside the Ar-filled glove box and then compacted into a cylindrical pellet using a hydraulic press. The pellet was again sealed in a carbon-coated fused evacuated silica tube and reheated at 1273 K for four days. Then the resulting pellet was crushed into a fine powder inside the glove box, and a part of the sample was analyzed by the powder X-ray diffraction study. The same heating profile was further successfully used to synthesize ~3 g of a polycrystalline sample.

2.2. Single-crystal X-ray diffraction study

A single crystal X-ray diffraction (SCXRD) data set was collected for an EDX analyzed $Y_3Fe_{0.5}SiSe_7$ crystal at RT using a Bruker D8 Venture diffractometer equipped with Photon III mixed mode detector. A graphite monochromatized Mo-$K\alpha$ ($\lambda = 0.71073$ Å) radiation source was used to collect the intensity data. A few EDX-analyzed crystals were first transferred into a small drop of Paratone – N oil on a glass plate. A suitable crystal was selected and mounted on an X-ray transparent loop. The loop was then affixed to a goniometer head to collect a fast scan of diffraction data to check the crystal quality. The operating voltage and current of the diffractometer were set to 50 kV and 1.5 mA, respectively. The exposure time, crystal-to-detector distance, and frame width values were fixed to 2 s/frame, 50 mm, and 0.5°, respectively. The ω and φ scans were used to collect the complete intensity data set. The data collection, cell constant refinements, and data integration were carried out with the help of the APEX3 software package [25]. The absorption corrections of the experimental reflections were performed using the multi-scan method implemented in the SADABS software [26].

A hexagonal primitive (P) cell was selected by the XPREP program [27], and only two compatible space groups were suggested: $P6_3/m$ (centrosymmetric) and $P6_3$ (chiral). The structure solution attempts using the centrosymmetric $P6_3/m$ space group failed. Further, the chiral $P6_3$ (no 173) space group was selected for the structure solution. The statics of intensity [$|E^2-1| \cong 0.72$] was also indicative of a non-centrosymmetric structure. The initial model of the crystal structure of $Y_3Fe_{0.5}SiSe_7$ was determined by the direct methods using the SHELXS program [28]. Six crystallographic independent atomic positions were identified and assigned to respective elements based on peak heights, coordination environments, and interatomic distances. The $Y_3Fe_{0.5}SiSe_7$ structure's model consisted of one Y, one Fe, one Si, and three
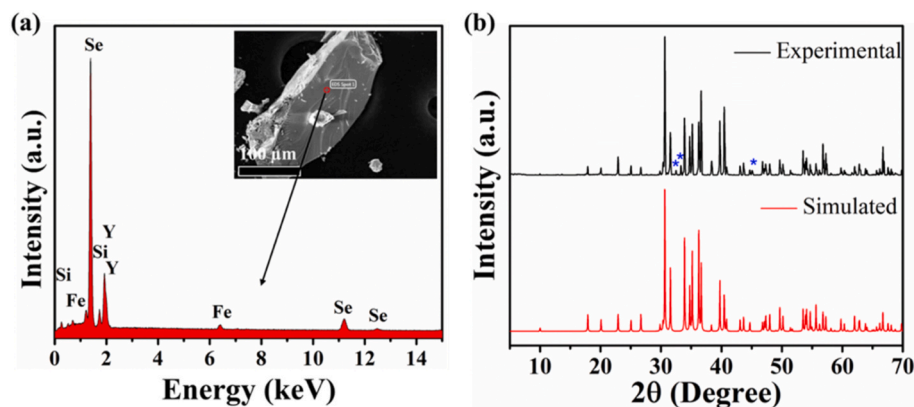
Fig. 1. (a) The EDX spectrum collected for a typical crystal of the $Y_3Fe_{0.5}SiSe_7$, and **(b)** a comparison of the simulated and experimental powder X-ray diffraction patterns of the polycrystalline $Y_3Fe_{0.5}SiSe_7$ sample. The asterisk (*) symbol shows the reflections of some unknown secondary phase(s).

independent Se sites. The isotropic thermal parameter of the Fe atom was relatively bigger. The site occupancy factor (SOF) refinements revealed an occupational disorder at the Fe site with a refined SOF value of 49.03%. The remaining sites did not show any vacancy when SOFs were refined freely. Further, the SOF value of the Fe site was fixed to 50%, resulting in a charge-balanced formula of $Y_3Fe_{0.5}SiSe_7$ with two formula units (Z) in the cell.

Finally, weight correction, anisotropic displacement parameters, scale factors, and extinction parameters were refined. The ADDSYM program [29] of the PLATON [29] did not detect any missing symmetry. A minimal residual electron density of 0.7 Å^{-3} was spotted at (0.0000, 0.0000, 0.7770), which is 1.33 Å apart from the Fe(1) atom. The deepest hole (-0.51 Å^{-3}) is present at (0.8425, 0.5326, 0.7011), which is 1.98 Å away from the Si(1) atom. Further pertinent crystallographic refinement details are provided in Tables 1-3, and in the supporting information (SI) file.

2.3. Powder X-ray diffraction (PXRD) study

The phase identification of the polycrystalline samples was performed by the PXRD studies. The PXRD data sets of the finely ground samples were collected at RT using a Rigaku Ultima IV diffractometer with Cu-$K\alpha$ radiation (λ = 1.5406 Å) source. The PXRD data were recorded over a 2θ range of 5°–70° using a $\theta - 2\theta$ geometry. The experimental PXRD patterns were compared with the theoretical PXRD patterns simulated from the single-crystal structural data. The *Match3!* software [30] was employed for the phase analyses of the PXRD patterns.

2.4. Solid-state ultraviolet–visible–near infrared (UV–Vis–NIR) spectroscopy

An optical absorption study of the polycrystalline sample of the $Y_3Fe_{0.5}SiSe_7$ was carried out at RT to determine the bandgap of the sample using a JASCO V-770 UV–Vis–NIR spectrophotometer. A dried powdered sample of $BaSO_4$ was used as a standard reference for the UV–Vis–NIR absorption study. The dataset was collected in a diffuse reflectance mode in the wavelength range of 2000 nm (0.62 eV) to 250 nm (4.96 eV). The reflectance data were transformed into absorption data using the Kubelka-Munk equation, $\alpha/S = (1 - R)^2/2R$. The absorption coefficient, scattering coefficient, and reflectance are represented by the symbols α, S, and R, respectively [31]. The absorption *vs.* energy plot was used to estimate the bandgap by absorption edge study. The nature of the bandgap and its value was calculated using the Tauc plot relation $(\alpha h\nu)^n = A(h\nu - E_g)$, where A is a proportionality constant, h is the Planck constant, ν is the frequency, and E_g represents the optical bandgap value [32]. Here the values of the constant n suggest the nature

of the bandgap (the n = ½ value implies an indirect bandgap, and a value of 2 indicates a direct bandgap).

2.5. Low-temperature resistivity study of the polycrystalline $Y_3Fe_{0.5}SiSe_7$

The direct current (DC) electrical resistivity study of the sintered $Y_3Fe_{0.5}SiSe_7$ pellet was carried out from 300 K to 195 K by the conventional four-probe method using a CCR-VTI system (CIA, USA). Four contacts of thin copper wire (0.05 mm diameter) were made on the rectangular pellet's surface using silver paste and dried in an inert atmosphere. The PXRD study of the sample after the resistivity measurements shows the sample was stable under the studied temperature.

2.6. Thermal conductivity study of the polycrystalline $Y_3Fe_{0.5}SiSe_7$

The thermal diffusivity (D) of a cylindrical (diameter = 8 mm) sintered pellet of the polycrystalline $Y_3Fe_{0.5}SiSe_7$ sample was studied using a LINSEIS XFA-500 system. The pellet was prepared by cold pressing the polycrystalline $Y_3Fe_{0.5}SiSe_7$ sample under a pressure of ~20 MPa using a hydraulic press and an 8 mm diameter stainless-steel die set. The prepared pellet was sintered at 873 K for 48 h inside a vacuum-sealed carbon-coated fused silica tube. A Xe flash was irradiated at the bottom of the graphite-coated sintered pellet to get the thermal diffusivity data at different temperatures. The thermal diffusivity (D) values were converted to total thermal conductivity ($k_{tot} = D \times d \times C_p$) values by multiplying them with the experimental density (d) and heat capacity (C_p) values. The density of the pellet was calculated using well known Archimedes method. It was ~90% of the theoretical density. The Dulong-petit law was used to calculate the heat capacity (C_p) value of 0.328 $Jg^{-1}K^{-1}$. The microstructure of the pellet was studied by the field emission scanning electron microscope (FE-SEM) with model number JSM 7800 F (Make: JEOL, Japan).

2.7. Theoretical and computational methodology

The density functional theory (DFT) [33] calculations are performed using the plane wave formalism as implemented in the VASP Package [34]. The Kohn-Sham single-particle wavefunctions are expanded on the basis of plane waves using the kinetic energy cutoff of 350 eV (or higher). The ionic core potentials are approximated using the projected augmented wave (PAW) pseudopotentials [35]. The $(4s^2, 4p^6, 5s^1, 4d^2)$, $(3d^6, 4s^2)$, $(3s^2, 3p^2)$, and $(4s^2, 4p^4)$ valence electron configurations are used for Y, Fe, Si, and Se atoms, respectively. The Perdew-Burke-Ernzerhoff (PBE) [36] form of the generalized gradient approximation (GGA) is used to include the exchange-correlation (XC) effects in the effective potential. In addition to the GGA scheme, the GGA-1/2 [37] and the meta-GGA XC schemes such as SCAN [38] and

mBJ [39] are also used to estimate the bandgap. The reciprocal space integrations are performed by sampling the Brillouin zone using the $(7 \times 7 \times 12)$ Monkhorst-Pack k-point mesh. The unit cells are relaxed and optimized by allowing the atomic Hellmann-Feynman forces to reduce up to ~0.02 eV/Å (or less). The total energies are allowed to converge up to 10^{-6} eV/cell to achieve self-consistency (SCF) in the calculations. For theoretical calculations, the $Y_3Fe_{0.5}SiSe_7$ structure is modeled by creating Fe vacancy at one of the two sites, i.e., (0, 0, 0) and (0, 0, 0.5). The linear optical properties are calculated from the electronic band structure within the independent-particle approximation [40]. The thermoelectric properties are calculated using the Boltzmann transport equations and rigid band approximation [41]. The procedures to compute optical and thermoelectric parameters are provided in the SI1 and SI2 sections, respectively of the SI file.

3. Results and discussion

3.1. Syntheses and crystal structure of the $Y_3Fe_{0.5}SiSe_7$

Black-colored crystals of the $Y_3Fe_{0.5}SiSe_7$ were synthesized at 1223 K by reacting stoichiometric amounts of elements inside an evacuated carbon-coated fused silica tube. The approximate yield of the crystals was 60%. The polycrystalline sample of the $Y_3Fe_{0.5}SiSe_7$ was also synthesized after establishing the structure and composition of the phase. Various heating profiles were explored, and the best quality polycrystalline sample was obtained by reacting stoichiometric amounts of elements at 1223 K using the two-step solid-state synthesis method described in section 2.1.2. The observed PXRD pattern of the polycrystalline product can be indexed satisfactorily with the corresponding simulated pattern obtained from the SCXRD study (Fig. 1b). A small amount of some unknown secondary phase(s) was also observed (Fig. 1b). Magnetic study of the polycrystalline sample was not studied due to presence of the trace of secondary phase(s). The refined unit cell parameters obtained from the Le Bail refinement of the PXRD data (see Fig. SI1 of the SI file) are $a = 10.201(1)$ Å and $c = 5.986(1)$ Å, which agree well with the constants calculated by the SCXRD study. The attempts to synthesize the Te-analog by reaction of elements at high temperatures were fruitless.

3.2. Crystal structure description of the $Y_3Fe_{0.5}SiSe_7$

The SCXRD study was used to determine the crystal structure of the $Y_3Fe_{0.5}SiSe_7$ phase. It crystallizes in the $Sm_3Fe_{0.5}SiSe_7$ [23] structure type with a noncentrosymmetric $P6_3$ space group with two formula units (Z). The unit cell dimensions of the structure are $a = b = 10.1971(1)$ Å, $c = 5.9799(2)$ Å, and $V = 538.49(2)$ Å^3. As expected, these unit cell dimensions are slightly bigger than the S-analog [42] due to the larger size of Se^{2-} than the S^{2-} ions [43]. The $Y_3Fe_{0.5}SiSe_7$ structure is non-stoichiometric with Fe vacancy. The asymmetric unit of the structure is composed of six crystallographically independent atomic positions (Table 2): one Y, one half-filled Fe, one Si, and three Se sites. Table 2 contains information on the site symmetry, Wyckoff positions, and site occupancies of these atomic sites. Only Fe1, Si1, and Se3 atoms are situated at the special positions in this structure.

The unit cell of the $Y_3Fe_{0.5}SiSe_7$ structure is presented in Fig. 2. Each Fe atom in the structure is bonded to six Se1 atoms forming a slightly distorted FeSe$_6$ octahedron with two sets of Fe–Se bonds. If one ignores the occupational disorder at the Fe site, each FeSe$_6$ unit shares two of its opposite Se faces with two neighboring Fe atoms, as shown in Fig. 3a, to form an infinite chain of $_{1}^{\infty}[Fe_2Se_6]^{8-}$ extending along the c-axis (Fig. 3d). However, half of the Fe atoms in these chains are randomly missing. Thus, the chain's composition in the $Y_3Fe_{0.5}SiSe_7$ structure is $_{1}^{\infty}[FeSe_6]^{10-}$. The Si atom in this structure is tetrahedrally connected to three Se2 atoms and one Se3 atom (Fig. 3c). The SiSe$_4$ tetrahedron does

not share its Se atoms with other neighboring Si-atoms.

The coordination number of each Y atom is also six, but the coordination geometry of the YSe$_6$ unit is a distorted trigonal prism (*TP*), as shown in Fig. 3b. This *TP* is made up of three Se1, two Se2, and one Se3 atoms. The Y–Se distances in the YSe$_6$ units are in the range of 2.8302(6) Å – 3.0358(6) Å. There are two more Se atoms (Se1 and Se2) close to the Y atom with Y–Se2 and Y–Se1 distances of 3.1270(6) Å and 3.3540(8) Å, respectively. These distances are relatively longer than the remaining Y–Se distances, as well as the sum of ionic radii of Y^{3+} (0.9 Å) and Se^{2-} (1.98 Å). The geometry around Y atoms can be described as a bicapped trigonal prism if these two Se atoms are also considered as a part of the coordination polyhedra of the Y atom. When the Y-atoms are filled in between the one-dimensional $_{1}^{\infty}[FeSe_6]^{10-}$ chains and discrete $[SiSe_4]^{4-}$ tetrahedra, the three-dimensional structure of the $Y_3Fe_{0.5}SiSe_7$ results.

The Fe–Se bond distances observed in the distorted octahedral FeSe$_6$ (2.689(2) Å to 2.699(2) Å) units can be compared with the corresponding distances in the related chalcogenide structures such as the $Gd_3FeGaSe_7$ (2.631(3) Å to 2.699(4) Å) [44], Fe_2GeSe_4 (2.495(8) Å to 2.730(6) Å) [45], and $Sm_3Fe_{0.5}SiSe_7$ (2.67(1) Å to 2.75(1) Å) [23]. The Si–Se distances of tetrahedral units are also in good agreement with corresponding bonds in the SiSe$_4$ units of the $BaZnSiSe_4$ (2.268(2) Å to 2.2995(19) Å) [46], $Na_2EuSiSe_4$ (2.246(2) Å to 2.288(2) Å) [47], and $Ce_3Mn_{0.5}SiSe_7$ (2.217(7) Å to 2.297(3) Å) [23]. The Y–Se distances in the YSe$_6$ unit vary from 2.8302(6) Å to 3.0358(6) Å and are consistent with those observed in the $Y_3CuSiSe_7$ (2.864(1) Å to 3.067(1) Å) [19], $CsYZnSe_3$ (2.8652(4) Å to 2.8641(3) Å) [48], and Ba_2GaYSe_5 (2.800(2) Å to 3.012(2) Å) [49] structures.

There are no short homoatomic interactions or short Y–Fe (or Si) and Fe–Si interactions in the crystal structure of the $Y_3Fe_{0.5}SiSe_7$. In this structure, the Y, Fe, Si, and Se atoms can be easily assigned to their most stable oxidation states of +(III), +(II), +(IV), and –(II), respectively. As a result, the charge-balanced formula is achieved as $(Y^{3+})_3(Fe^{2+})_{0.5}(Si^{4+})_1(Se^{2-})_7$.

Structural relationships of the $Y_3Fe_{0.5}SiSe_7$ with known related structures.

The $Y_3Fe_{0.5}SiSe_7$ structure is closely related to the $Ln_3M_{1-\delta}TtQ_7$ (Ln = lanthanides and Y; M = Fe, Mn, and Cu; and Tt = tetrels = Si, Ge, and Sn; Q = S and Se; δ = 0 or 0.5) structures [18–23]. Regardless of the metal or metalloid atoms in this structure type, all crystallize in the hexagonal $P6_3$ space group. The occupancy of the M site in the Ln_3MTtSe_7 structure varies as a function of its oxidation state. The divalent Mn^{2+} or Fe^{2+} site in this structure type is only half-occupied, whereas the Cu-analogs (with Cu^{1+} ions) do not show such occupational disorder. Although the space groups of all these compounds are the same, they offer primarily two types of structures (Fig. 4) depending on the coordination environment of M atoms. The monovalent copper atoms occupy trigonal planar sites in contrast to the divalent Fe or Mn atoms which sit at the distorted octahedral sites. Both these structure

Table 2
Fractional atomic coordinates and U_{iso}/U_{eq} values for the $Y_3Fe_{0.5}SiSe_7$ structure.

Atoms	Wyckoff Position	Site symmetry	SOF	x	y	z	U_{iso}/U_{eq} [a]
Y1	6c	1	1	0.35789(4)	0.22196(5)	0.20892(9)	0.01045(11)
Fe1	2a	3..	0.5	0.000000	0.000000	−0.0017(6)	0.0139(5)
Si1	2b	3..	1	0.666667	0.333333	0.6226(4)	0.0078(4)
Se1	6c	1	1	0.09726(5)	0.25163(5)	0.24684(10)	0.01087(11)
Se2	6c	1	1	0.57719(5)	0.47833(4)	0.47109(9)	0.00857(11)
Se3	2b	3..	1	0.666667	0.333333	0.99817(15)	0.00873(16)

[a] U_{iso}/U_{eq} is the one-third value of the trace of orthogonalized U_{ij} tensor.

Table 3
Selected interatomic lengths (Å) for the $Y_3Fe_{0.5}SiSe_7$ structure.

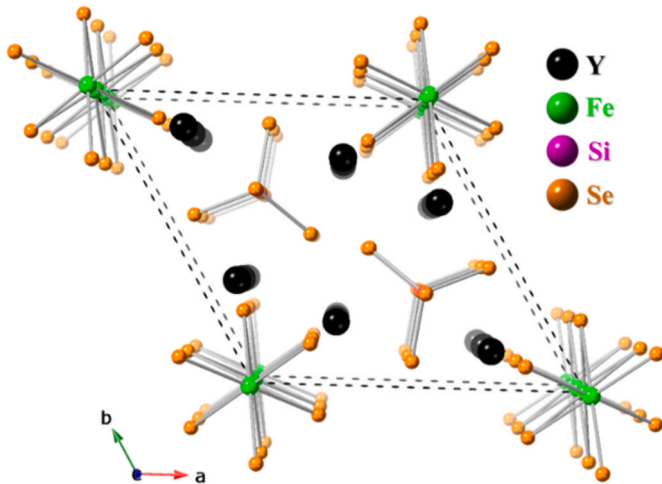| Atomic pair	Bond distance (Å)	Atomic pair	Bond distance (Å)
Y1 − Se1	2.8302(6)	Fe1 − Se1	2.689(2) × 3
Y1 − Se1	2.8634(6)	Fe1 − Se1	2.699(2) × 3
Y1 − Se1	2.9219(8)	Si1 − Se3	2.246(2)
Y1 − Se1	3.3540(8)	Si1 − Se2	2.278(1) × 3
Y1 − Se2	2.9063(6)	Y⋯Y	4.3724(2)
Y1 − Se2	2.9865(7)	Fe⋯Fe	2.9898(2)
Y1 − Se2	3.1270(6)	Si⋯Si	5.9799(6)
Y1 − Se3	3.0358(6)	Se⋯Se	3.4897(6)

Fig. 2. A view of the unit cell of the $Y_3Fe_{0.5}SiSe_7$ structure along the [001] direction. The Y–Se bonds are omitted for clarity.

types, $Ln_3(Fe/Mn)_{0.5}TtQ_7$ and Ln_3CuTtQ_7, are derived from the $Ce_6Al_{3.33}S_{14}$ structure type [50]. The comparison of these structure types is presented in Fig. 4.

In $Ln_3(Fe/Mn)_{0.5}TtQ_7$ structures, the transition metal (Fe or Mn) forms an octahedral coordination geometry with its surrounding Se atoms and creates an infinite one-dimensional $_1^\infty[FeSe_6]^{10-}$ by face-sharing. However, when Fe^{2+}/Mn^{2+} species, which are half-occupied, are replaced by monovalent Cu^{1+}, the octahedral chain gets disturbed, and Cu^{1+} forms a discrete triangular planner geometry with its surrounding Se atoms. These discrete $CuSe_3$ units are extended along the c-axis in a staggered fashion, as shown in Fig. 4b. The Tt atoms form distorted tetrahedra in all these structures Ln_3MTtQ_7. Each Y or Ln atom in the Ln_3MTtQ_7 structure is coordinated with six Se atoms and forms a TP-like polyhedron. Thus, the oxidation state of the M atoms and their coordination environments determines the structure type of the Ln_3MTtQ_7 family: La_3CuSiS_7 [51] *vs.* $Ce_6Al_{3.33}S_{14}$ [50] or $Sm_3Fe_{0.5}SiSe_7$ [23].

3.3. Optical bandgap study of the polycrystalline $Y_3Fe_{0.5}SiSe_7$

The finely ground polycrystalline sample of the $Y_3Fe_{0.5}SiSe_7$ was used for the optical absorption study at RT. The direct bandgap of the sample was calculated using the Tauc plot, as shown in Fig. 5a.

The direct bandgap for the $Y_3Fe_{0.5}SiSe_7$ was found to be 1.1(1) eV, indicating the material's narrow bandgap semiconducting nature. The black color of the sample also agrees with the observed bandgap value.

3.4. The resistivity study of the polycrystalline $Y_3Fe_{0.5}SiSe_7$

We next present the temperature-dependent resistivity (ρ) study of the sintered pellet of the $Y_3Fe_{0.5}SiSe_7$ sample. As expected for a semiconducting sample, the resistivity value starts to increase on cooling the sample. The electrical resistivity of the sample is 100 Ω m at RT (300 K), which further exponentially increased to 120 kΩ m at 195 K. The resistivity data below 195 K could not be collected due to the sample's high-insulating behavior. To calculate the activation energy, we used the Arrhenius plot (inset of Fig. 5b) of $\ln(\rho)$ vs.$1/k$T (in eV^{-1}), where the symbol k represents the Boltzmann constant. The Arrhenius plot revealed a nearly straight line in the temperature range of 200 K–270 K. Based on the slope of this line, the activation energy was estimated to be around 0.2(1) eV. The presence of the small amount of the unknown secondary phase(s) in the $Y_3Fe_{0.5}SiSe_7$ sample is expected to hamper the true value of the electrical resistivity to some extent. Nevertheless, the observed semiconducting nature of the sample from the resistivity study corroborates the optical study and theoretical electronic structure (see section 3.6) of the $Y_3Fe_{0.5}SiSe_7$.

3.5. Thermal conductivity study of the polycrystalline $Y_3Fe_{0.5}SiSe_7$

The thermal conductivity of the polycrystalline cylindrical sintered pellet was calculated over a temperature range of 323 K–773 K. Fig. 6a shows the thermal conductivity (k_{tot}) plot as a function of temperature (K). The value of k_{tot} is found to be inversely proportional to the temperature, and its value gradually decreased on heating the sample from 0.53 $Wm^{-1}K^{-1}$ at 323 K to an ultralow thermal conductivity value of ~0.26 $Wm^{-1}K^{-1}$ at 773 K. The k_{tot} value of any crystalline sample is the summation of the two terms, electronic (k_e) and lattice or phonon (k_l) components of total thermal conductivity k_{tot}. The high resistivity value of the polycrystalline sample suggests that the contribution of k_e is minimal to the k_{tot} values. As discussed earlier, the $Y_3Fe_{0.5}SiSe_7$ structure is disordered due to a 50% vacancy at the Fe site in its structure. Such disorder in the structure is usually expected to enhance the phonon-phonon scattering at high temperatures, leading to a decrease in the k_l value. A small amount of the unknown secondary phase could also have some contribution to the total thermal conductivity of the polycrystalline sample of the $Y_3Fe_{0.5}SiSe_7$. Future temperature-dependent Raman studies on a phase pure sample of the $Y_3Fe_{0.5}SiSe_7$ will be useful to elucidate the role of phonon-phonon interactions for the realization of low k_{tot} value of the structure.

The thermal conductivity of the polycrystalline $Y_3Fe_{0.5}SiSe_7$ sample at 773 K can be compared to other metal chalcogenides such as $Ba_4Mn_2Si_2Te_9$ (~0.45 W/mK at 773 K) [52], SnSe (~0.5 W/mK at 750 K) [53], $BaSb_2Se_4$ (~0.29 W/mK at 773 K) [54], and
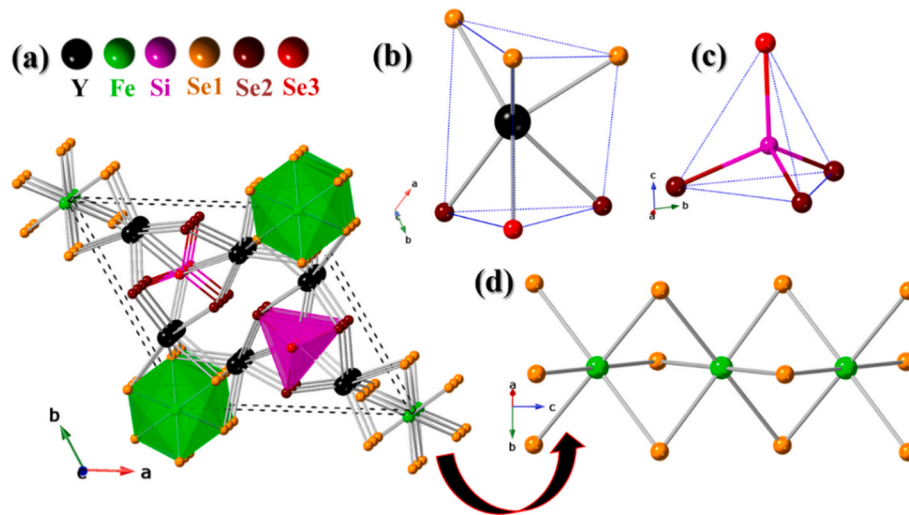
Fig. 3. (a) The 3D structure of the $Y_3Fe_{0.5}SiSe_7$ unit cell viewed along the *c*-axis, the coordination environments of the **(b)** Y atom, **(c)** Si atom, and **(d)** a polyhedral view of the $FeSe_6$ units along the [001] direction.
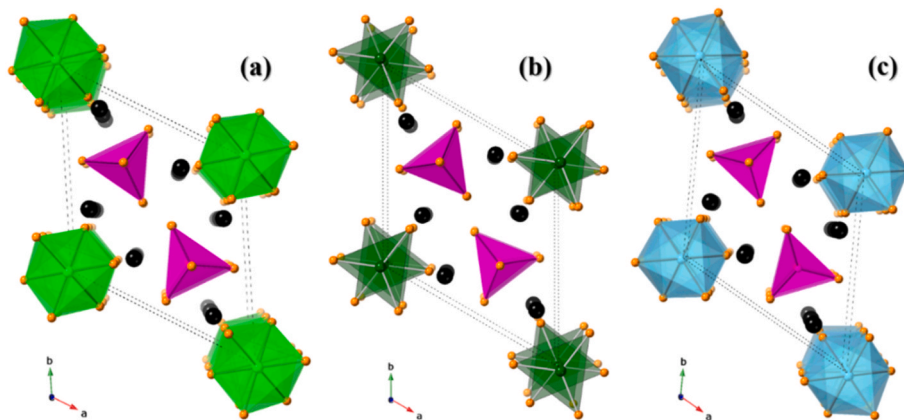

Fig. 4. The polyhedral models of the unit cell of the **(a)** $Y_3Fe_{0.5}SiSe_7$, **(b)** $Y_3CuSiSe_7$ [19], and **(c)** $Sm_3Fe_{0.5}SiSe_7$ [23] structures.
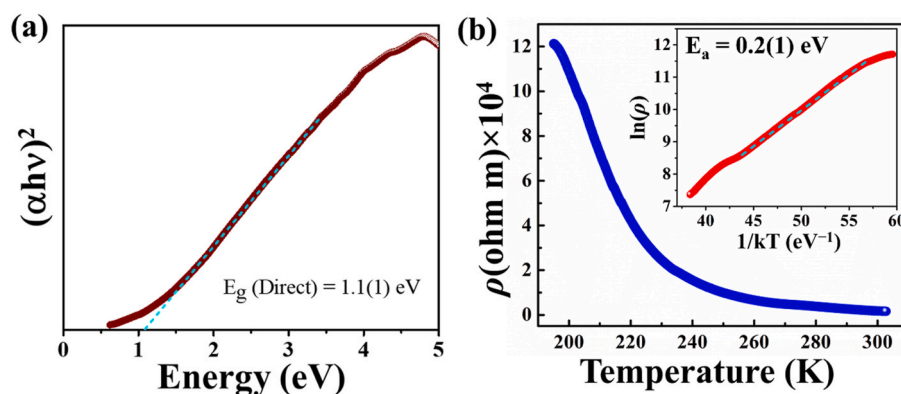

Fig. 5. (a) The direct bandgap Tauc plot and **(b)** the temperature-dependent resistivity (inset activation energy plot) plot for the polycrystalline $Y_3Fe_{0.5}SiSe_7$.

$Cu_{1.7}Ag_{0.3}Se_{0.85}S_{0.15}$ (~0.34 W/mK at 500 K) [55].

The FE-SEM technique was used to examine the microstructure of the fractured surface of the polycrystalline $Y_3Fe_{0.5}SiSe_7$ pellet used for thermal conductivity measurements (Fig. 6b). The pellet is found to be reasonably dense with some tiny pores, as can be seen in the FE-SEM micrographs (Fig. 6b). Also, we do not see any preferential ordering of grains in this sample from the FE-SEM analysis.

The low value of $k_{tot} = $ ~0.26 $Wm^{-1}K^{-1}$ at 773 K is beneficial from the thermoelectric point of view. However, the poor electrical conductivity of the sample is detrimental to achieving any reasonable thermoelectric figure of merit (*zT*) in this material (see section 3.6.3 for details of the *zT*). The electrical conductivity of this sample could be improved by substituting Si with Ge atoms. These studies will be carried out in the future to explore doped samples of $Y_3Fe_{0.5}SiSe_7$ for *TE*
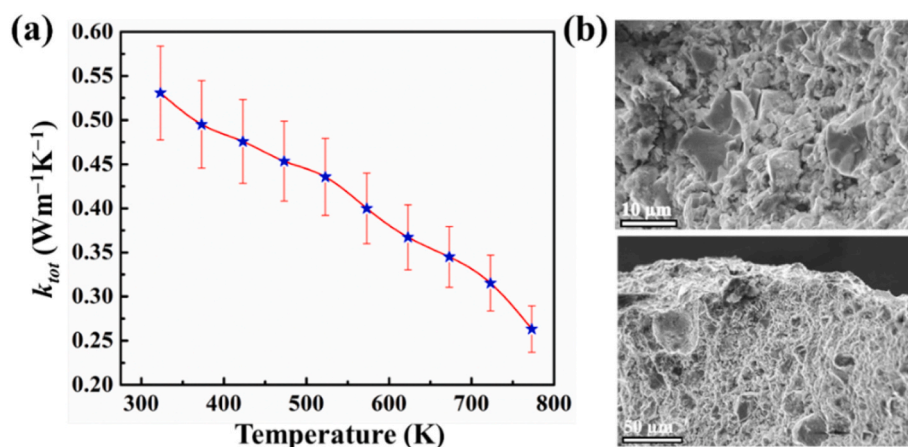
Fig. 6. (a) The temperature-dependent thermal conductivity plot of the polycrystalline $Y_3Fe_{0.5}SiSe_7$ sample, and **(b)** the FE-SEM images of the fractured pellet of the $Y_3Fe_{0.5}SiSe_7$ sample.

applications.

3.6. Theoretical studies of the $Y_3Fe_{0.5}SiSe_7$

3.6.1. Electronic structure of the $Y_3Fe_{0.5}SiSe_7$

Next, we present the computed unit cell parameters of the $Y_3Fe_{0.5}SiSe_7$ structure and discuss its electronic structure in detail. The experimental values of the lattice parameters and atomic positions augur well (within $\sim 0.02\%$) with their corresponding computed values (Table 4). The computed lattice parameters using the GGA and LDA schemes show the expected trend. As can be seen, these values computed using the GGA and LDA schemes yield slightly overestimated and underestimated values, respectively, as expected [40].

The bandgap values for the $Y_3Fe_{0.5}SiSe_7$ structure computed using the GGA and LDA are ~ 0.76 eV and ~ 0.72 eV, respectively. In general, the bandgaps of the semiconductors (insulators) are systematically underestimated as much as by $\sim 50\%$ as compared to the experimental values when computed using local or semi-local approximations such as the LDA and GGA. Indeed, the calculated bandgap values using the GGA and LDA schemes are significantly smaller than the experimental value of ~ 1.1 eV. Interestingly, the bandgap value computed using the SCAN (meta-GGA) scheme comes out to be 1.15 eV which is in good agreement with the experimental value. The SCAN scheme fulfills all known constraints required for any exact density functional and therefore is expected to provide a better estimate of bandgap than GGA and LDA schemes. On the other hand, the bandgap values computed using the mBJ and GGA-1/2 schemes are ~ 1.96 eV and ~ 0.70 eV, respectively. As evident, the mBJ scheme overestimates the bandgap value of the $Y_3Fe_{0.5}SiSe_7$ structure, whereas the GGA-1/2 scheme underestimates the same. Though mBJ and GGA-1/2 schemes are known to provide better estimates of bandgap values, these schemes fail to perform any better in comparison to the GGA in the present case of the $Y_3Fe_{0.5}SiSe_7$.

Next, we explore the electronic structure of the $Y_3Fe_{0.5}SiSe_7$ by analyzing the density of states (DOS) and band structure plots, as shown in Fig. 7. In the DOS plot (see Fig. 7a), the valence band maximum

(VBM) is at 0 eV, and the conduction band minimum (CBM) is present at ~ 0.8 eV. The valence band (VB) in the ~ -0.5 eV $< E < 0$ eV energy region is formed primarily due to semi-localized Fe-3d states. The VB in the lower energy range (~ -6 eV $< E < -0.9$ eV) energy region results primarily due to the overlap of Se-4p and Fe-3d states, along with a smaller contribution from Si-2p and Y-4d states. The localized Si-2s states can be seen in the VB region at ~ -8 eV. The localized Se-4s states are mainly responsible for the VB in the ~ -14 eV $< E < -12.5$ eV energy region. In the conduction band (CB), the sharp peak at CBM at ~ 0.8 eV is due to Fe-3d states. The CB in the higher energy range (~ 0.9 eV $< E < 6$ eV) is primarily comprised of the Y-4d states, along with a smaller contribution from the Fe-3d states. The band structure shown in Fig. 7b suggests that the electronic bandgap is direct since both the VBM and CBM are at A-point (0, 1/2, 1/2) in the Brillouin zone.

As mentioned earlier, two possible models of the $Y_3Fe_{0.5}SiSe_7$ structure are considered for theoretical calculations. These are generated by creating Fe vacancy at sites (0, 0, 0) and (0, 0, 0.5), respectively. The lattice parameters, bandgaps, and electronic structures computed using these two models are found to be almost identical.

3.6.2. The computed projected crystal orbital Hamilton populations (COHP) and bader charges

Next, we present the COHP [56] values for the pertinent atom contacts in the $Y_3Fe_{0.5}SiSe_7$ structure. These COHP values are an indicator of the relative strength and nature of bonding between different atoms of the structure. The COHP plot as a function of energy (E) for the Y − Se, Fe − Se, and Si − Se bonding pairs is shown in Fig. 8a. In general, the sign of the COHP (E) provides information on the nature of bonding between atom pairs: a positive sign of COHP (E) is indicative of bonding interaction while negative sign suggests antibonding interactions. Fig. 8b shows the magnitudes of the ICOHP or integrated COHP values obtained by integrating the COHP (E) up to the VBM. The ICOHPs magnitudes shed light on the relative strengths of the bonding between atom pairs. As evident from Fig. 8b, the strength of the Si − Se bond is highest in the $Y_3Fe_{0.5}SiSe_7$ structure, followed by the Y − Se and Fe − Se bonds.

Next, we compute the Bader charges (Q_B) on the Y, Fe, Si, and Se ions in the $Y_3Fe_{0.5}SiSe_7$ structure. These charges help to qualitatively estimate the relative charges transferred between atoms during bonding [57]. The Bader charges are useful to ascertain the relative degree of covalent and ionic character of the bonding interaction between two atoms. The Q_B values of the Y, Fe, Si, and Se ions are computed to be +1.85, +0.5, +1.77, and −1.1, respectively. The magnitudes of these charges clearly indicate that the charge (electron) is transferred from the more electropositive Y, Fe, and Si atoms to the electronegative Se atoms, resulting in a predominantly ionic type of bonding. The electron

Table 4
The lattice parameters and bandgap (eV) values of the $Y_3Fe_{0.5}SiSe_7$ computed using various XC schemes (GGA, LDA, SCAN, mBJ, and GGA-1/2).

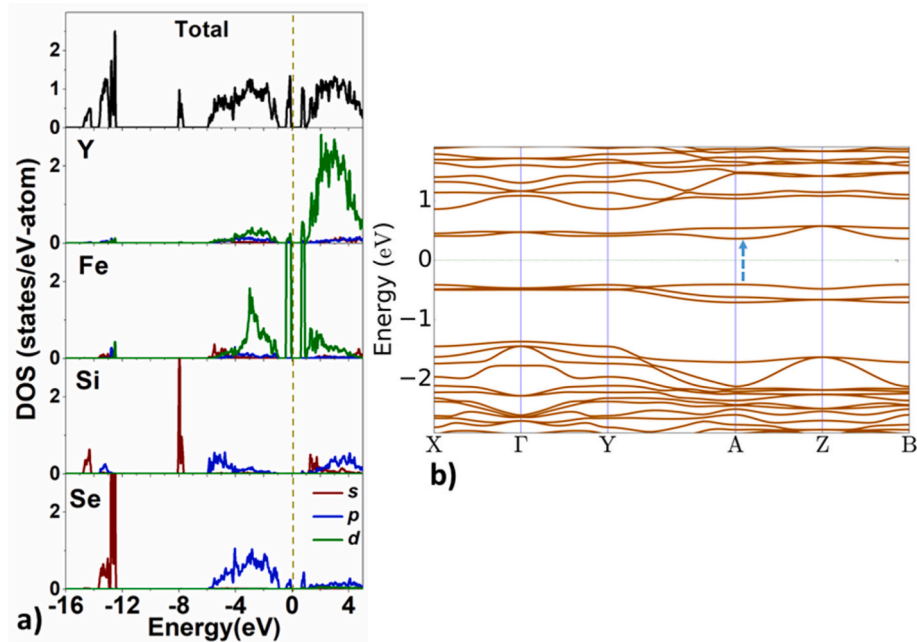|		$a = b(\text{Å})$	$c(\text{Å})$	$V(\text{Å}^3)$	$E_g(\text{eV})$
Cal.	GGA	10.2189	6.0143	543.89	0.76
	LDA	9.9803	5.8464	5.40.32	0.72
	SCAN	–	–	–	1.15
	mBJ	–	–	–	1.96
	GGA-1/2	–	–	–	0.70
Exp.		10.1971	5.9799	538.49	1.1(1)

Fig. 7. (a) The total and projected density of states (DOS) and **(b)** the band structure for the $Y_3Fe_{0.5}SiSe_7$. The vertical dotted line indicates the valence band maximum in Fig. 7a. $X \equiv \left(\frac{1}{2},0,0\right)$, $\Gamma \equiv (0,0,0)$, $Y \equiv \left(0,\frac{1}{2},0\right)$, $A \equiv \left(0,\frac{1}{2},\frac{1}{2}\right)$, $Z \equiv \left(0,0,\frac{1}{2}\right)$, $B \equiv \left(\frac{1}{2},0,\frac{1}{2}\right)$ are the high symmetry k-points in the Brillouin zone.
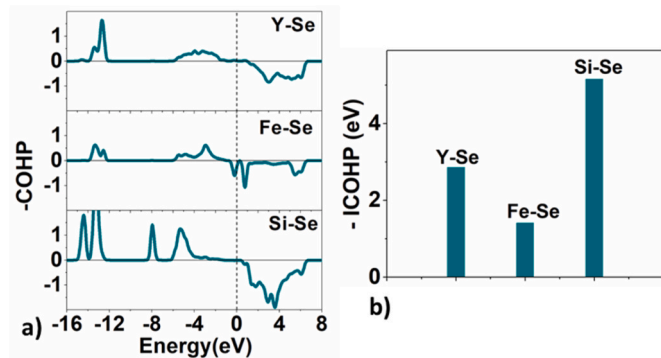

Fig. 8. (a) The crystal orbital Hamilton population (COHP) and the **(b)** integrated COHP values for the $Y - Se$, $Fe - Se$, and $Si - Se$ bonds in the $Y_3Fe_{0.5}SiSe_7$ structure.

localization function (ELF) plots [58] (Fig. SI2 of the SI file) are also helpful in visualizing the electron transfer from the metals to the Se atoms in the $Y_3Fe_{0.5}SiSe_7$ structure. The computed Q_B values are smaller than the formal oxidation state of $+$(III), $+$(II), $+$(IV), and $-$ (II) for the Y, Fe, Si, and Se, respectively, in the title structure. This may suggest the presence of a minor degree of the covalent character of the bonds between the Se atoms and the Y, Fe, and Si atoms though the bonding is

primarily ionic due to charge transfer. In particular, some degree of directional covalent bonding can be seen for the $Si - Se$ bonds in the ELF plot shown in Fig. SI2 of the SI file.

3.6.3. Theoretical optical and thermoelectric properties

The optical parameters are computed from frequency-dependent complex dielectric function $\varepsilon(\omega) = \varepsilon' + i\varepsilon''$, which in turn is computed from electronic band structure (see section SI1 of the SI file). The onset of the imaginary part of the dielectric function (ε'') indicates the optical bandgap as it is related to absorption. The absorption coefficient α, αE, and $(\alpha E)^2$ values are plotted as a function of photon energy (E) and shown in Fig. 9. The magnitude of α value rises in the optical region and attains a maximum value around $\sim$4.5 eV. Overall, the features of the computed absorption coefficient plot are consistent with the experimental plot shown in Fig. 5a. One may note that the theoretical optical properties are derived from band-to-band transitions and thus include the contribution of single-particle electronic band structure only.

Furthermore, we use the electronic band structure of the $Y_3Fe_{0.5}SiSe_7$ to compute the thermoelectric parameters such as the thermoelectric figure of merit (zT), Seebeck coefficient (S), etc. The $zT \propto \frac{1}{(k_e + k_l)}$ where k_e and k_l are the electronic and lattice (phonon) components of total thermal conductivity k_{tot}. In our calculations, k_l is treated as an external parameter with values taken from the experimental plot shown in Fig. 7a.

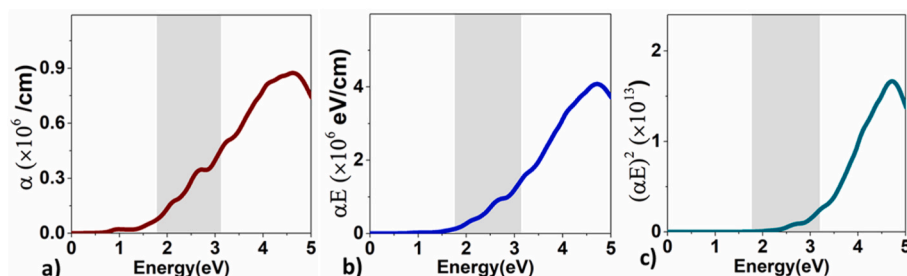According to the Wiedemann-Franz relation, the electronic compo-

Fig. 9. The plots of the **(a)** α, **(b)** (αE), and **(c)** $(\alpha E)^2$ values as a function of energy (E) for the $Y_3Fe_{0.5}SiSe_7$. The α symbol represents the absorption coefficient.

nent of the thermal conductivity (k_e) and electrical conductivity (σ) values are related as $k_e = L_0 \sigma T$, where $L_0 = \frac{\pi^2}{3}\left(\frac{k_B}{e}\right)^2 = (156 \, \mu V/K)^2$ is the Lorentz number. The σ and k_e are computed with respect to the relaxation time $\tau = 10^{-14}$s. The temperature dependence of τ is also used using a simple approximation: $\tau(T) = (T_0/T) \times 10^{-14}$s, where $T_0 = 300$ K. We present the computed thermoelectric properties as a function of temperature and carrier concentration in Fig. 10. The Seebeck coefficient (S) and zT values for hole-doped $Y_3Fe_{0.5}SiSe_7$ as a function of hole concentrations at temperatures 300 K, 500 K, and 800 K are shown in Fig. 10. As evident from the plot of S *vs.* hole concentration, the $|S|$ values vary in the range $\sim 900 > S > 100 \, \mu V/K$ for carrier (hole) concentration $\sim 10^{17} < p < 10^{21}$ cm^{-3}. Qualitatively similar variation is found for *n*-doped $Y_3Fe_{0.5}SiSe_7$. The Seebeck coefficient (S) can be seen to rise with increasing concentration or temperature as expected. Using the nearly free electrons, parabolic band, and energy-independent scattering approximation [59], the Seebeck coefficient values vary with the temperature (T), carrier concentration (p), and carrier effective mass (m^*) as $S \propto \frac{m^* T}{p^{2/3}}$. The zT value (Fig. 10b) initially enhances with carrier concentration, attaining a maximum value at $\sim p = 5 \times 10^{20}$ cm^{-3}, and after that, it decreases. The maximum value of zT also rises on increasing the temperature as expected. It may be noted that the direct comparison of the *ab-initio* thermoelectric parameters with the experiments may be ambiguous and tricky as these parameters can critically depend on the value of the carrier concentration in the sample that may in turn depend on other parameters such as sample quality, microstructure, etc. Nevertheless, the present theoretical estimates of the *TE* parameters of the $Y_3Fe_{0.5}SiSe_7$ would be useful to understand the correlation between the intrinsic dependences of these parameters and the electronic band structure.

4. Conclusions

The crystals of the Fe-deficient $Y_3Fe_{0.5}SiSe_7$ were synthesized at 1223 K by the sealed tube method. The SCXRD study determined the crystal structure of the $Y_3Fe_{0.5}SiSe_7$. It crystallizes in the hexagonal $P6_3$ space group with the unit cell parameters of $a = b = 10.1971(1)$ Å, $c = 5.9799(2)$ Å, $V = 538.49(2)$ Å^3, and $Z = 2$. The asymmetric unit of the structure contains six crystallographically independent atomic positions one Y, one Fe, one Si, and three Se sites. The Fe site is half-occupied. The octahedral $FeSe_6$ units and tetrahedral $SiSe_4$ units are the main building block of this structure, and Y atoms are filled in between these Fe and Si-centered polyhedra to form the trigonal prism-like geometry of YSe_6. The optical absorption study on the polycrystalline $Y_3Fe_{0.5}SiSe_7$ established the semiconducting nature with a direct bandgap of 1.1(1) eV. The low-temperature resistivity study also verified the semiconducting nature of the material. The thermal conductivity value of the polycrystalline $Y_3Fe_{0.5}SiSe_7$ was found to be gradually decreasing on heating the sample with an extremely low value of $\sim$0.26 W/mK at 773 K. The *ab-initio* study of electronic structure, optical, and thermoelectric properties of the $Y_3Fe_{0.5}SiSe_7$ is also performed within the framework of DFT. The theoretical bandgap is computed using different XC functions, and their performances vis-à-vis bandgap estimation are assessed. The computed COHP values of the pertinent atom pairs in the $Y_3Fe_{0.5}SiSe_7$ structure reveal the strongest bonding between Si and Se than the Y − Se and Fe − Se pairs.

Credit author statement

GP and SY carried out the synthesis, crystal structure determinations, powder X-ray diffraction studies, SEM and EDX analysis, and thermal conductivity. SJ has carried out the UV–Vis–NIR diffuse reflectance measurement studies. MS and SA carried out low temperature resistivity studies. MKN has performed the electronic structure calculations. All authors contributed to the final manuscript. After getting input from all authors, GP, MKN, and JP wrote the manuscript. JP was involved in
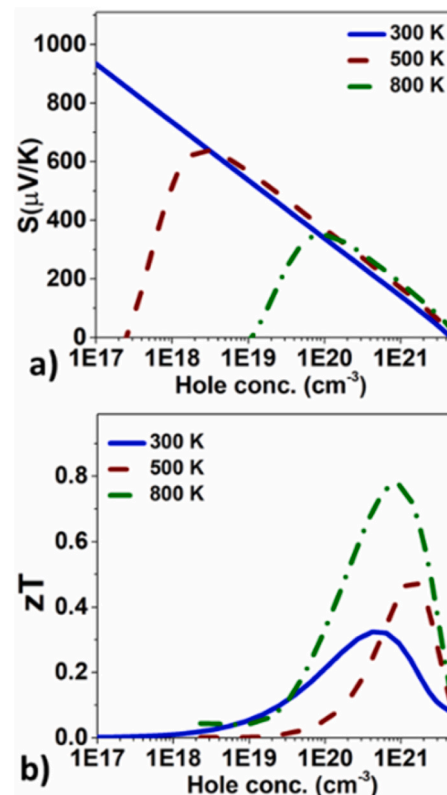

Fig. 10. (a) The Seebeck coefficient (μV /K) values and **(b)** the zT values as a function of carrier concentration for the hole-doped $Y_3Fe_{0.5}SiSe_7$.

conceptualization, overall guidance, data analysis, writing, reviewing, and editing the manuscript.

Declaration of competing interest

The authors declare that they have no known competing financial interests or personal relationships that could have appeared to influence the work reported in this paper.

Data availability

Data will be made available on request.

Acknowledgments

Appendix A. Supplementary data

Supplementary data to this article can be found online at https://doi.org/10.1016/j.solidstatesciences.2023.107133.

References

[1] A.K. Iyer, J. He, H. Xie, D. Goodling, D.-Y. Chung, V. Gopalan, M.G. Kanatzidis, Stabilization of the polar structure and giant second-order nonlinear response of single crystal γ-NaAs$_{0.95}$Sb$_{0.05}$Se$_2$, Adv. Funct. Mater. (2022), 2211969, https://doi.org/10.1002/adfm.202211969.

[2] C.C. Laing, B.E. Weiss, K. Pal, M.A. Quintero, H. Xie, X. Zhou, J. Shen, D.Y. Chung, C. Wolverton, M.G. Kanatzidis, ACuZrQ$_3$ (A = Rb, Cs; Q = S, Se, Te): direct bandgap semiconductors and metals with ultralow thermal conductivity, Chem. Mater. 34 (2022) 8389–8402, https://doi.org/10.1021/acs.chemmater.2c02104.

[3] A.A. Berseneva, V.V. Klepov, K. Pal, K. Seeley, D. Koury, J. Schaeperkoetter, J. T. Wright, S.T. Misture, M.G. Kanatzidis, C. Wolverton, A.V. Gelis, H.-C. zur Loye, Transuranium sulfide via the boron chalcogen mixture method and reversible water uptake in the NaCuTS$_3$ family, J. Am. Chem. Soc. 144 (2022) 13773–13786, https://doi.org/10.1021/jacs.2c04783.

[4] T.K. Bera, J.I. Jang, J.B. Ketterson, M.G. Kanatzidis, Strong second harmonic generation from the tantalum thioarsenates A$_3$Ta$_2$AsS$_{11}$ (A = K and Rb), J. Am. Chem. Soc. 131 (2009) 75–77, https://doi.org/10.1021/ja807928d.

[5] M.E. Maldonado, A. Das, A.M. Jawaid, A.J. Ritter, R.A. Vaia, D.A. Nagaoka, P. G. Vianna, L. Seixas, C.J.S. de Matos, A. Baev, P.N. Prasad, A.S.L. Gomes, Nonlinear optical interactions and relaxation in 2D layered transition metal dichalcogenides probed by optical and photoacoustic Z-scan methods, ACS Photonics 7 (2020) 3440–3447, https://doi.org/10.1021/acsphotonics.0c01327.

[6] M.-M. Chen, S.-H. Zhou, W. Wei, M.-Y. Ran, B. Li, X.-T. Wu, H. Lin, Q.-L. Zhu, RbBiP$_2$S$_6$: a promising ir nonlinear optical material with a giant second-harmonic generation response designed by aliovalent substitution, ACS Materials Lett 4 (2022) 1264–1269, https://doi.org/10.1021/acsmaterialslett.2c00409.

[7] M.-Y. Li, B. Li, H. Lin, Z. Ma, L.-M. Wu, X.-T. Wu, Q.-L. Zhu, Sn$_2$Ga$_2$S$_5$: a polar semiconductor with exceptional infrared nonlinear optical properties originating from the combined effect of mixed asymmetric building motifs, Chem. Mater. 31 (2019) 6268–6275, https://doi.org/10.1021/acs.chemmater.9b02389.

[8] C. Li, W. Yin, P. Gong, X. Li, M. Zhou, A. Mar, Z. Lin, J. Yao, Y. Wu, C. Chen, Trigonal planar [HgSe$_3$]$^{4-}$ unit: a new kind of basic functional group in ir nonlinear optical materials with large susceptibility and physicochemical stability, J. Am. Chem. Soc. 138 (2016) 6135–6138, https://doi.org/10.1021/jacs.6b03107.

[9] Y. Chi, Z.-D. Sun, Q.-T. Xu, H.-G. Xue, S.-P. Guo, Hexagonal In$_2$Se$_3$: a defect wurtzite-type infrared nonlinear optical material with moderate birefringence contributed by unique InSe$_5$ unit, ACS Appl. Mater. Interfaces 12 (2020) 17699–17705, https://doi.org/10.1021/acsami.9b23085.

[10] S.-P. Guo, G.-C. Guo, M.-S. Wang, J.-P. Zou, G. Xu, G.-J. Wang, X.-F. Long, J.-S. Huang, A series of new infrared NLO semiconductors, ZnY$_6$Si$_2$S$_{14}$, Al$_x$Dy$_3$(Si$_y$Al$_{1-y}$)S$_7$, and Al$_{0.33}$Sm$_3$SiS$_7$, Inorg. Chem. 48 (2009) 7059–7065, https://doi.org/10.1021/ic802443n.

[11] S. Jana, M. Ishtiyak, L. Govindaraj, S. Arumugam, B. Tripathy, S.K. Malladi, M. K. Niranjan, J. Prakash, Metal to insulator transition in Ba$_2$Ge$_2$Te$_5$: synthesis, crystal structure, resistivity, thermal conductivity, and electronic structure, Mater. Res. Bull. 147 (2022) 111641–111651, https://doi.org/10.1016/j.materresbull.2021.111641.

[12] M.-M. Chen, Z. Ma, B.-X. Li, W.-B. Wei, X.-T. Wu, H. Lin, Q.-L. Zhu, M$_2$As$_2$Q$_5$ (M = Ba, Pb; Q = S, Se): a source of infrared nonlinear optical materials with excellent overall performance activated by multiple discrete arsenate anions, J. Mater. Chem. C 9 (2021) 1156–1163, https://doi.org/10.1039/D0TC05952H.

[13] H. Chen, W.-B. Wei, H. Lin, X.-T. Wu, Transition-metal-based chalcogenides: a rich source of infrared nonlinear optical materials, Coord. Chem. Rev. 448 (2021) 214154–214192, https://doi.org/10.1016/j.ccr.2021.214154.

[14] G. Panigrahi, S. Yadav, S. Jana, K.V. Ramanujachary, M. Niranjan, J. Prakash, Ba$_4$FeAgS$_6$: a new antiferromagnetic and semiconducting quaternary sulfide, Dalton Trans. 52 (2023) 621–634, https://doi.org/10.1039/D2DT03209K.

[15] M. Ishtiyak, S. Jana, R. Karthikeyan, R. Mamindla, B. Tripathy, S.K. Malladi, M. Niranjan, J. Prakash, Syntheses of five new layered quaternary chalcogenides SrScCuSe$_3$, SrScCuTe$_3$, BaScCuSe$_3$, BaScCuTe$_3$, and BaScAgTe$_3$: crystal structures, thermoelectric properties, and electronic structures, Inorg. Chem. Front. 8 (2021) 4086–4101, https://doi.org/10.1039/D1QI00717C.

[16] W. Wang, H. Yang, M. Luo, Y. Zhong, D. Xu, T. Wu, Z. Lin, A 36-membered ring metal chalcogenide with a very low framework density, Inorg. Chem. 56 (2017) 14730–14733, https://doi.org/10.1021/acs.inorgchem.7b02109.

[17] S. Margadonna, Y. Takabayashi, M.T. McDonald, K. Kasperkiewicz, Y. Mizuguchi, Y. Takano, A.N. Fitch, E. Suard, K. Prassides, Crystal structure of the new FeSe$_{1-x}$ superconductor, Chem. Commun. (2008) 5607–5609, https://doi.org/10.1039/b813076k.

[18] B.W. Rudyk, S.S. Stoyko, A.O. Oliynyk, A. Mar, Rare-earth transition-metal gallium chalcogenides RE$_3$MGaCh$_7$ (M = Fe, Co, Ni; Ch = S, Se), J. Solid State Chem. 210 (2014) 79–88, https://doi.org/10.1016/j.jssc.2013.11.003.

[19] L.D. Gulay, O.S. Lychmanyuk, J. Stępień-Damm, A. Pietraszko, I.D. Olekseyuk, Crystal structures of the Y$_3$CuSiS$_7$ and Y$_3$CuSiSe$_7$ compounds, J. Alloys Compd. 402 (2005) 201–203, https://doi.org/10.1016/j.jallcom.2005.04.146.

[20] Y.-F. Shi, Y. Chen, M.-C. Chen, L.-M. Wu, H. Lin, L.-J. Zhou, L. Chen, Strongest second harmonic generation in the polar R$_3$MTQ$_7$ family: atomic distribution induced nonlinear optical cooperation, Chem. Mater. 27 (2015) 1876–1884, https://doi.org/10.1021/acs.chemmater.5b00177.

[21] L.D. Gulay, O.S. Lychmanyuk, M. Wołcyrz, A. Pietraszko, I.D. Olekseyuk, The crystal structures of R$_3$CuGeS$_7$ (R = Ce–Nd, Sm, Gd–Dy and Er), J. Alloys Compd. 425 (2006) 159–163, https://doi.org/10.1016/j.jallcom.2006.01.056.

[22] H. Chen, M.-Y. Ran, W.-B. Wei, X.-T. Wu, H. Lin, Q.-L. Zhu, A comprehensive review on metal chalcogenides with three-dimensional frameworks for infrared nonlinear optical applications, Coord. Chem. Rev. 470 (2022) 214706–214740, https://doi.org/10.1016/j.ccr.2022.214706.

[23] J. He, Z. Wang, X. Zhang, Y. Cheng, Y. Gong, X. Lai, C. Zheng, J. Lin, F. Huang, Synthesis, structure, magnetic and photoelectric properties of Ln$_3$M$_{0.5}$M′Se$_7$ (Ln = La, Ce, Sm; M = Fe, Mn; M′ = Si, Ge) and La$_3$MnGaSe$_7$, RSC Adv. 5 (2015) 52629–52635, https://doi.org/10.1039/C5RA05629B.

[24] K.M. Poduska, L. Cario, F.J. DiSalvo, K. Min, P.S. Halasyamani, Structural studies of a cubic, high-temperature (α) polymorph of Pb$_2$GeS$_4$ and the isostructural Pb$_{2-x}$Sn$_x$GeS$_{4-y}$Se$_y$ solid solution, J. Alloys Compd. 335 (2002) 105–110, https://doi.org/10.1016/S0925-8388(01)01836-9.

[25] APEX3, Program for Data Collection on Area Detectors, Bruker AXS Inc., Madison, WI, USA, 2016.

[26] G.M. Sheldrick, SADABS, Department of Structural Chemistry, University of Göttingen, Göttingen, Germany, 2008.

[27] G.M. Sheldrick, XPREP Version 2008/2, Bruker AXS Inc., Madison, 2018.

[28] G.M. Sheldrick, Acta Crystallogr. A 64 (2008) 112–122.

[29] A.L. Spek, Single-crystal structure validation with the program PLATON, J. Appl. Crystallogr. 36 (2003) 7–13, https://doi.org/10.1107/S0021889802022112.

[30] New match! Version 3.13 (build 227). https://www.crystalimpact.com/news/20220314b.htm.

[31] G. Kortüm, Reflectance Spectroscopy: Principles, Methods, Applications, Springer-Verlag, Berlin Heidelberg, 1969, https://doi.org/10.1007/978-3-642-88071-1.

[32] P. Makuła, M. Pacia, W. Macyk, How to correctly determine the band gap energy of modified semiconductor photocatalysts based on UV–vis spectra, J. Phys. Chem. Lett. 9 (2018) 6814–6817, https://doi.org/10.1021/acs.jpclett.8b02892.

[33] W. Kohn, L.J. Sham, Self-consistent equations including exchange and correlation effects, Phys. Rev. 140 (1965) A1133–A1138.

[34] G. Kresse, J. Furthmüller, Efficient iterative schemes for ab initio total-energy calculations using a plane-wave basis set, Phys. Rev. B 54 (1996) 11169–11186, https://doi.org/10.1103/PhysRevB.54.11169.

[35] P.E. Blöchl, Projector augmented-wave method, Phys. Rev. B 50 (1994) 17953–17979, https://doi.org/10.1103/PhysRevB.50.17953.

[36] J.P. Perdew, K. Burke, M. Ernzerhof, Generalized gradient approximation made simple, Phys. Rev. Lett. 77 (1996) 3865–3868, https://doi.org/10.1103/PhysRevLett.77.3865.

[37] L.G. Ferreira, M. Marques, L.K. Teles, Approximation to density functional theory for the calculation of band gaps of semiconductors, Phys. Rev. B 78 (2008) 125116–125125, https://doi.org/10.1103/PhysRevB.78.125116.

[38] J. Sun, A. Ruzsinszky, J.P. Perdew, Strongly constrained and appropriately normed semilocal density functional, Phys. Rev. Lett. 115 (2015), 036402, https://doi.org/10.1103/PhysRevLett.115.036402, 036408.

[39] F. Tran, P. Blaha, Accurate band gaps of semiconductors and insulators with a semilocal exchange-correlation potential, Phys. Rev. Lett. 102 (2009) 226401, https://doi.org/10.1103/PhysRevLett.102.226401, 22645.

[40] R.M. Martin, R.M. Martin, Electronic Structure: Basic Theory and Practical Methods, Cambridge University Press, 2004.

[41] G.K.H. Madsen, J. Carrete, M.J. Verstraete, BoltzTraP2, a program for interpolating band structures and calculating semi-classical transport coefficients, Comput. Phys. Commun. 231 (2018) 140–145, https://doi.org/10.1016/j.cpc.2018.05.010.

[42] G. Collin, P. Laruelle, Crystal structure of La$_6$MnSi$_2$S$_{14}$, C. R. Seances Acad. Sci., Ser. C 270 (1970) 410–412.

[43] L. Pauling, Atomic radii and interatomic distances in metals, J. Am. Chem. Soc. 69 (1947) 542–553, https://doi.org/10.1021/ja01195a024.

[44] W. Yin, W. Wang, L. Kang, Z. Lin, K. Feng, Y. Shi, W. Hao, J. Yao, Y. Wu, Ln$_3$FeGaQ$_7$: a new series of transition-metal rare-earth chalcogenides, J. Solid State Chem. 202 (2013) 269–275, https://doi.org/10.1016/j.jssc.2013.03.029.

[45] J.A. Henao, J.M. Delgado, M. Quintero, X-ray powder diffraction data and structural study of Fe$_2$GeSe$_4$, Powder Diffr. 13 (1998) 196–201, https://doi.org/10.1017/S0885715600010101.

[46] W. Yin, A.K. Iyer, C. Li, J. Yao, A. Mar, Noncentrosymmetric chalcogenides BaZnSiSe$_4$ and BaZnGeSe$_4$ featuring one-dimensional structures, J. Alloys Compd. 708 (2017) 414–421, https://doi.org/10.1016/j.jallcom.2017.03.009.

[47] A. Choudhury, P.K. Dorhout, An ordered assembly of filled nanoscale tubules of europium seleno-silicate in the crystal structure of a quaternary compound, J. Am. Chem. Soc. 129 (2007) 9270–9271, https://doi.org/10.1021/ja073335q.

[48] K. Mitchell, C.L. Haynes, A.D. McFarland, R.P. Van Duyne, J.A. Ibers, Tuning of optical band gaps: syntheses, structures, magnetic properties, and optical properties of CsLnZnSe$_3$ (ln = Sm, Tb, Dy, Ho, Er, Tm, Yb, and Y), Inorg. Chem. 41 (2002) 1199–1204, https://doi.org/10.1021/ic011200u.

[49] W. Yin, K. Feng, W. Wang, Y. Shi, W. Hao, J. Yao, Y. Wu, Syntheses, structures, optical and magnetic properties of Ba$_2$MLnSe$_5$ (M = Ga, in; ln = Y, Nd, Sm, Gd, Dy, Er), Inorg. Chem. 51 (2012) 6860–6867, https://doi.org/10.1021/ic300604a.

[50] D. De Saint-Giniez, P. Laruelle, J. Flahaut, C.R., Structure cristalline du sulfure double de cerium et d'aluminium Ce$_6$Al$_{3.333}$S$_{14}$, C. R. Seances Acad. Sci., Ser. C 267 (1968) 1029–1032.

[51] M. Guittard, M. Julien-Pouzol, Hexagonal compounds of the La$_3$CuSiS$_7$ type, Bull. Soc. Chim. Fr. 7 (1970) 2467–2469.

[52] S. Yadav, S. Jana, G. Panigrahi, S.K. Malladi, M.K. Niranjan, J. Prakash, Five coordinated Mn in Ba$_4$Mn$_2$Si$_2$Te$_9$: synthesis, crystal structure, physical properties, and electronic structure, Dalton Trans. 51 (2022) 9265–9277, https://doi.org/10.1039/D2DT01167K.

[53] L.-D. Zhao, S.-H. Lo, Y. Zhang, H. Sun, G. Tan, C. Uher, C. Wolverton, V.P. Dravid, M.G. Kanatzidis, Ultralow thermal conductivity and high thermoelectric figure of merit in SnSe crystals, Nature 508 (2014) 373–377, https://doi.org/10.1038/nature13184.

[54] S. Jana, G. Panigrahi, G. Ummethala, A. Ghosh, S.K. Malladi, M.K. Niranjan, J. Prakash, Extremely low thermal conductivity in $BaSb_2Se_4$: synthesis, characterization, and DFT studies, J. Solid State Chem. 315 (2022) 123524–123535, https://doi.org/10.1016/j.jssc.2022.123524.

[55] M. Guan, K. Zhao, P. Qiu, D. Ren, X. Shi, L. Chen, Enhanced thermoelectric performance of quaternary $Cu_{2-2x}Ag_{2\ x}Se_{1-\ x}S_x$ liquid-like chalcogenides, ACS Appl. Mater. Interfaces 11 (2019) 13433–13440, https://doi.org/10.1021/acsami.9b01643.

[56] V.L. Deringer, A.L. Tchougréeff, R. Dronskowski, Crystal orbital Hamilton population (COHP) analysis as projected from plane-wave basis sets, J. Phys. Chem. A 115 (2011) 5461–5466, https://doi.org/10.1021/jp202489s.

[57] W. Tang, E. Sanville, G. Henkelman, A grid-based Bader analysis algorithm without lattice bias, J. Phys. Condens. Matter 21 (2009), 084204, https://doi.org/10.1088/0953-8984/21/8/084204, 084211.

[58] B. Silvi, A. Savin, Classification of chemical bonds based on topological analysis of electron localization functions, Nature 371 (1994) 683–686, https://doi.org/10.1038/371683a0.

[59] G.J. Snyder, E.S. Toberer, Complex thermoelectric materials, Nat. Mater. 7 (2008) 105–114, https://doi.org/10.1038/nmat2090.